Simulation of Wind Profiles from a Space-borne Doppler Wind Lidar

By G.J. MARSEILLE * and A. STOFFELEN
KNMI, The Netherlands

SUMMARY

The importance of wind observations for meteorological analysis has been recognized for many years. The current global observing system lacks a uniform distribution of tropospheric wind measurements, especially in the tropics, southern hemisphere, and northern hemisphere oceans. A Doppler wind lidar (DWL), mounted on a space-borne platform, has the potential to provide a global three-dimensional coverage of wind data. The European Space Agency (ESA) has decided to fly a DWL on a polar orbiting satellite platform in 2007 as part of the Atmospheric Dynamics Mission (ADM) called Aeolus. The proposed DWL is a non-scanning single perspective instrument, operating in the ultraviolet part of the electromagnetic spectrum, providing profiles of line-of-sight (LOS) wind components from detected light backscattered from the illuminated atmospheric volume. The concept has been simulated and was used in observation system simulation experiments (OSSE) to assess its potential impact on numerical weather prediction and climate processes. This paper describes the simulation of Aeolus LOS wind component profiles and its expected quality in cloud-free and cloudy conditions

KEYWORDS: Atmospheric Dynamics Mission - Aeolus Cloud penetration Direct detection Line-of-sight wind component

1. INTRODUCTION

The quality of state-of-the-art numerical weather prediction (NWP) is critically dependent on the quantity and quality of meteorological observations. NWP models have improved much over the last decades and advanced 4D-var techniques are now being used for the analysis. Moreover, long series of such analyses (e.g. from the ECMWF re-analysis project) are these days widely used for research on climate processes. The spatial resolution of global circulation models (GCM) has as well improved, which leads to a need for more observations on the sub-synoptic scales. On these smaller scales wind observations become relatively more important than mass (temperature) observations (ESA 1999). Despite the growing amount of wind observations from space such as cloud motion wind vectors, water vapour motion wind vectors, scatterometer and from aircraft reports, the radiosonde observation network still constitutes the backbone for wind profile information (e.g. ESA 1999). Figure 1 shows many wind profile data void areas on the globe, in particular over the oceans. The World Meteorological Organisation (WMO) has stated that measurement of wind profiles remains most challenging and most important for global meteorological analyses (WMO 2001). Wind profile measurements from space by a Doppler Wind Lidar (DWL) may contribute to fill in the gaps in the global observing system (GOS).

Experiments with existing observing systems, denoted OSE, have shown that good coverage of wind observations is essential to ensure that "precursive" features are represented in the numerical weather prediction (NWP) analyses. DWL winds should therefore bring a major improvement to the subsequent NWP forecasts of cyclogenesis (Graham and Anderson 1996; Kelly 1997). Atmospheric structures that are "precursors" to the development of extra-tropical cyclones can often be identified before cyclogenesis takes place. Examples are small-scale wave-like disturbances in the jet stream or vertically tilted (baroclinic) structures.

* KNMI, Postbus 201, 3730 AE De Bilt, The Netherlands, e-mail: Gert-Jan.Marseille@knmi.nl
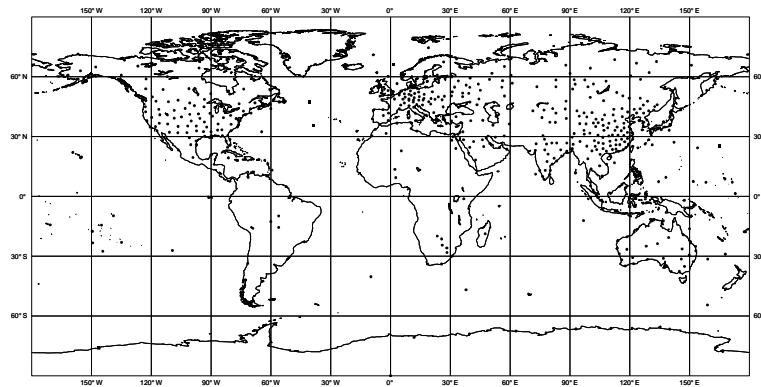
Figure 1.   Typical coverage of wind profile data from the radiosonde observation network. Note the low density in the southern hemisphere, tropics and northern hemisphere oceans.

Besides utility for NWP, it is expected that a DWL would provide essential information to describe climatological processes such as the improvement of the Hadley circulation definition in the Tropics, water vapour fluxes in the hydrological cycle, transport of trace gases and aerosols (ESA 1996, 1999).

Within the context of the core earth explorer programme, as part of the ADM, the European Space Agency (ESA) is building a DWL aiming at observing the atmospheric wind field. Trade-off studies have resulted in a space-borne lidar concept that was approved by ESA as a demonstration mission and is expected to be operational in 2007 (ESA 1999). Its main component is a Doppler Wind Lidar, operating in the ultraviolet (UV) part of the electromagnetic spectrum at 0.355 μm laser wavelength, mounted on a polar orbiting satellite. A comprehensive introduction to lidar-measured winds from space is given by Baker (1995). Simulation of space-borne lidar measured winds with incoherent detection is discussed in Abreu (1979). The principle of lidar-measured wind profiles is discussed in section 2. The instrument configuration and atmospheric conditions such as the distribution of aerosols, molecules and clouds and their optical properties determine the quality of retrieved wind profiles. Simulation of realistic atmospheric conditions is discussed in section 3. Simulation of instrument characteristics such as detection and sampling of the atmosphere backscattered signal and signal post-processing to retrieve wind profiles are discussed in section 4. We show that Aeolus HLOS wind profiles meet the WMO accuracy requirement in cloud-free conditions. This includes retrieval in cloudy conditions. Section 5 shows that the Aeolus sampling strategy enables wind retrieval in cloudy conditions such as optically thin cirrus clouds and scenes of broken clouds.

2.   LIDAR PRINCIPLE

A lidar (acronym for light detection and ranging) emits laser pulses into the atmosphere. As the pulse propagates through the atmosphere, part of the signal is scattered back to the instrument by atmospheric particles that are moving with the wind velocity. These moving particles cause the frequency of the backscattered signal to be Doppler shifted with respect to the transmitted signal. The time lag between the transmitted and received signal determines the range of the scattering particle to the instrument. The frequency shift, Δf, is related directly to the wind velocity along the

laser beam line-of-sight, denoted v_{LOS}, according to

$$v_{\mathrm{LOS}} = \frac{\lambda}{2}\Delta f, \tag{1}$$

with λ the laser wavelength. The wind vector in the horizontal plane along the laser beam line-of-sight is denoted the horizontal line-of-sight (HLOS) wind component v_{HLOS}

$$v_{\mathrm{HLOS}} = -u\sin(\psi) - v\cos(\psi), \tag{2}$$

with u and v the horizontal wind components in the west-east and south-north direction respectively and ψ the azimuth angle, defined as the angle (clockwise) between the laser beam direction and geographical north. Neglecting vertical wind velocities (Lorenc *et al.*1992), v_{LOS} is the projection of v_{HLOS} on the laser line-of-sight in the vertical plane

$$v_{\mathrm{HLOS}} = \frac{v_{\mathrm{LOS}}}{\sin(\tilde{\phi})}, \tag{3}$$

with $\tilde{\phi}$ the local incidence angle, i.e. the angle between the incoming laser light beam and the normal at the earth surface. Sampling of the targeted volume from a single viewing angle does not resolve the complete wind vector. This requires illumination from several viewing angles, making the instrument more complex. However, for assimilation purposes in NWP models, the complete wind vector is not required. A single line-of-sight wind component can be assimilated as well providing half the information of the full wind vector (Lorenc *et al.*1992). This property in conjunction with the simple linear relationship between the measured quantity (frequency shift) and NWP model parameters (wind vector) through the equations above makes assimilation of DWL measurements straightforward.

3. ATMOSPHERIC BACKSCATTER AND TRANSMISSION

The capability of a space-borne Doppler wind lidar to measure wind profiles is mainly determined by the number of scattering particles in the atmosphere and their optical properties. For a laser operating in the UV we distinguish between backscatter from aerosols and molecules. Aerosol backscatter shows large variability over the globe, due to among others volcanic eruptions, dust storms, sea spray, industry and meteorological factors such as air mass stratification, convection, movement of air masses, rain depletion, etc. For simulation of realistic aerosol backscatter we used the climatological database of lidar measurements at 10.6μm laser wavelength that is the result of extensive measurement campaigns for regions of the Atlantic during the relatively clean atmospheric period 1988-1990 (Vaughan 1998). The results have been condensed in percentile profiles in Fig. 2 and indeed show a large variability of several orders of magnitude. A scaling law has been developed to convert to aerosol backscatter at $\lambda = 0.355\mu$m based on a manifold of campaign data and available literature (Vaughan *et al.*1998)

$$\beta_{\mathrm{a}}(\lambda, z) = \beta_0(z)\left(\frac{\lambda_0}{\lambda}\right)^{\alpha(\beta_0(z))}, \quad \alpha(\beta_0(z)) = -0.104\times\ln(\beta_0(z)) - 0.62, \tag{4}$$

with $\beta_0(z)$ aerosol backscatter at altitude z for a laser operating at $\lambda_0 = 10.6\mu$m wavelength, see Fig. 2.

As the laser light penetrates the atmosphere, part of the signal is lost by absorption and scattering of particles. At 0.355μm signal extinction through scattering is most
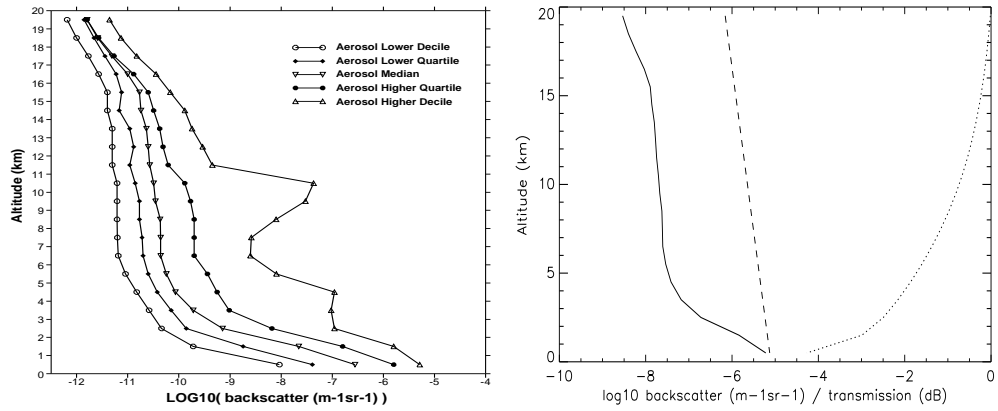
Figure 2. Left, aerosol backscatter ($m^{-1}sr^{-1}$) statistics at 10.6μm laser wavelength for cloud-free atmospheres derived from extensive measurement campaigns for regions of the Atlantic during the relatively clean atmospheric period 1988-1990. Aerosol backscatter shows a large variability of several orders of magnitude. Peaks in the higher decile are due to optically thin cirrus clouds. Right, typical atmospheric characteristics at 0.355μm laser wavelength. The solid line shows the aerosol backscatter profile, derived from the median profile in the left figure and the scaling law Eq. 4. The dashed line shows molecular backscatter and the dotted line the 10 log one-way atmospheric transmission in dB.

significant and depends on particle shape and size. We modelled aerosol extinction, α_a, assuming a constant aerosol backscatter-to-extinction coefficient $b_a(\lambda) = 0.02sr^{-1}$ (Vaughan *et al.*1998; Winker *et al.*1996), $\alpha_a(\lambda, z) = \beta_a(\lambda, z)/b_a(\lambda)$, with $\beta_a(\lambda, z)$ derived from Eq. (4). Unlike aerosols, molecules are well mixed in the atmosphere with fairly constant concentrations over the globe at each pressure level. Signal extinction through molecular scattering may be theoretically determined from the Rayleigh scattering law and knowledge of the atmospheric temperature and pressure (Reagan 1989). Molecular backscatter is related to molecular extinction through a backscatter-to-extinction coefficient $b_m(\lambda) = 3/8\pi$ sr^{-1}, hence $\beta_m(\lambda, z) = \alpha_m(\lambda, z)b_m(\lambda)$.

Clouds play a crucial role in the performance of a space-borne DWL. Opaque clouds generally hamper the laser beam to reach the underlying atmosphere. Transparent clouds such as thin cirrus yield a strong return signal and yet transmit a significant part of the laser beam. The cloud liquid-water content (CLW) and the size distribution of cloud droplets quantify the cloud penetrating capability of the laser beam. We modelled cloud extinction by Stephens (1984)

$$\alpha_{cld}(\lambda, z) = \frac{3 \times 10^{-6}}{2} \frac{CLW(z)\rho(z)}{\rho_l(z)r_e} \text{ with } r_e = \left(-3.8 \times 10^{-2} P + 43.8\right) 10^{-6} \quad (5)$$

which states that cloud extinction is inversely proportional to the mean effective radius, r_e, of the size distribution of the cloud droplets. The parameterization on the right-hand side of Eq. (5) has been adopted from the ECMWF forecast model and states that the mean size in low-level clouds is smaller than in high level clouds, making low-level clouds optically denser. In Eq. (5), ρ is the air density, ρ_l the density of liquid-water, and P is the air pressure in mb. Cloud backscatter is modelled by a constant backscatter-to-extinction ratio of $b_{cld}(\lambda) = 0.055$ sr^{-1} (Vaughan 1998) hence $\beta_{cld}(\lambda, z) = \alpha_{cld}(\lambda, z)b_{cld}(\lambda)$. The one-way atmospheric transmission of laser light, τ, between the satellite and the observed atmospheric layer at altitude z is derived from

aerosol, molecular and cloud extinction through

$$\tau(\lambda, z) = \exp\left[\frac{-1}{\cos(\tilde{\phi})} \int_z^{z_{\mathrm{atm}}} \left\{\alpha_{\mathrm{a}}(\lambda, z') + \alpha_{\mathrm{m}}(\lambda, z') + \alpha_{\mathrm{cld}}(\lambda, z')\right\} \mathrm{d}z'\right], \quad (6)$$

where z_{atm} denotes the top of atmosphere. For the simulations we set z_{atm} at 20 km and assume no signal loss above 20 km, which is slightly optimistic since ozone at higher altitudes absorbs a small part of the signal energy. Figure 2 displays typical atmospheric backscatter and transmission profiles at 0.355μm for a cloud-free atmosphere.

4. THE ATMOSPHERIC DYNAMICS MISSION

The main objective of the Atmospheric Dynamics Mission (ADM) is to improve understanding of the atmospheric dynamics and global atmospheric transport of energy, water, aerosols and chemicals. The mission main component is a Doppler wind lidar mounted on a satellite platform. The satellite will fly in a sun-synchronous dawn-dusk orbit at an altitude of 400 km and an inclination angle of 97.2 degrees, hence covering almost the full globe. Several trade-off studies have resulted in a lidar concept operating in the ultra-violet part of the electromagnetic spectrum at 0.355μm laser wavelength with a fixed line-of-sight pointing towards the atmosphere at 35 degrees off-nadir and 90 degrees across the satellite ground track on the earth surface, away from the sun (ESA 1999). This eliminates otherwise induced frequency shifts from the satellite speed relative to the illuminated atmosphere. Moreover, variability of vertical wind-shear, that is an important precursor for baroclinic instability (e.g. Hoskins 1990), is most dominant in the zonal direction (Marseille 1998). Hence, optimal shear visibility is accomplished by a sideward pointing lidar on a polar orbiting satellite. The 35 degrees look-angle is a compromise between HLOS wind retrieval from the measured Doppler shifted frequency minimum range from the satellite to the atmosphere and minimum cloud obstruction. Penetration of the lower troposphere in cloudy conditions is reduced only marginally at 35 degrees off-nadir with a maximum reduction of 10% at 50% cloud cover (Rapp 1973).

(a) Coverage or accuracy

In line with the objective of ADM, we focus on retrieval of HLOS wind components that can easily be assimilated in current NWP models as outlined in section 2. Wind observations should be obtained over an atmospheric volume that is representative of the global NWP analysis resolution i.e. about 50 km horizontally and 1 km vertically. A single shot retrieved point wind profile is not representative for the mean wind in the targeted sample volume and a substantial observation spatial representativeness error (Lorenc 1992) has to be taken into account. Dividing the available energy over spatially distributed laser shots in the targeted volume makes the retrieved wind profile more representative of the mean wind and thus reduces the representativeness error contribution. As such, the laser emits laser pulses into the atmosphere during 7 seconds at a laser pulse frequency of 100 Hz that is needed to obtain the required wind profile accuracy. For a satellite flying at a speed of about 7 km s^{-1} this corresponds to 50 km satellite displacement along track. Since power is an important limitation for space-borne DWL systems, it is important to use it effectively. As such, every single measured wind profile should contribute to resolve an independent analysis error structure. As a result of this consideration the lidar is inactive for 21 seconds after a
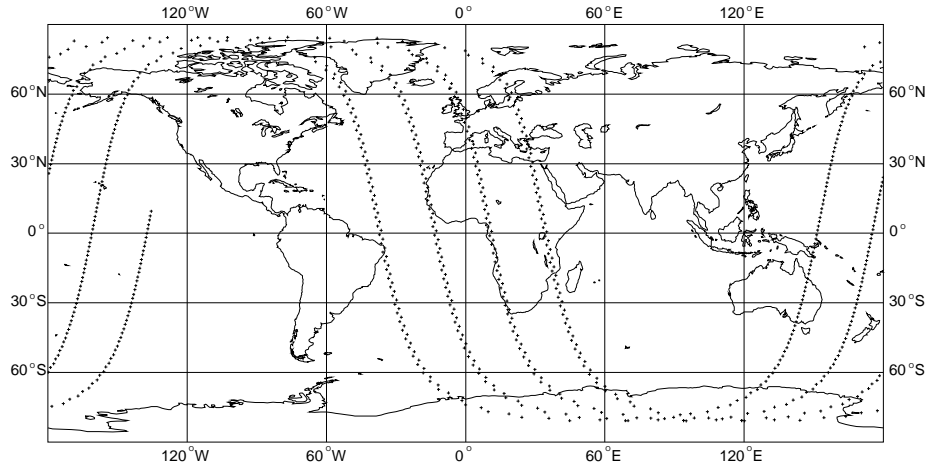
Figure 3. 6-hour data coverage of DWL single line-of-sight wind profiles, according to the ESA Atmospheric Dynamics Mission. Subsequent wind profile locations are separated by approximately 200 km.

wind profile observation is made, yielding a 25% duty cycle. The resulting horizontal distance between subsequent lidar wind profiles is 200 km, which corresponds roughly to the spatial correlation length of error structure functions in state-of-the-art GCMs. To simulate the horizontal sampling of the ADM concept we adopted the locations of the simulated conical scan DWL scenarios in the ECMWF OSSE database (Becker *et al.* 1996). The 6-hour simulated coverage in Fig. 3 does closely match the ADM coverage with a profile separation of 210 kilometers on average.

The return signal from the atmosphere is divided in sequential time intervals. The interval length determines the vertical (range gate) resolution of the retrieved wind profile. We simulated vertical wind profiles ranging from the earth surface up to 20 km altitude at 1000 meter resolution. This agrees well with the separation of vertical levels in current meteorological models and typical error correlation lengths of about 2000 meter. For technical reasons we did not simulate ADM in the height range 20-26 km, but performance assessment is rather straightforward in the lower stratosphere. The considerations above on coverage and accuracy are well covered by the WMO requirements on wind profile measurements in Table 1 (WMO 2001).

(b) Spectral distribution of atmospheric return signal

The spectral shape of the emitted UV laser pulses is assumed Gaussian with a standard deviation that corresponds to about 4 m s^{-1} for a laser operating at 0.355μm. Interaction of light with relatively large aerosol particles falls within the Mie scattering regime, while the relatively small molecules produce Rayleigh scattering (Reagan, 1989). Aerosol and cloud particles exhibit generally a negligible variability of movement, much smaller than the width of the laser pulse. Hence, the Mie spectral shape is determined by the laser spectrum. Molecules are subject to much larger Brownian motion and have greatly dispersed speeds according to a Gaussian distribution. Their variability of movement is a function of temperature T and the standard deviation ranges from about 258 m s^{-1} at 216K, i.e. at about 20 km altitude, to 300 m s^{-1} at 300K. The spectral distribution of atmospheric scattering particles at altitude z is a superposition of the Mie and Rayleigh spectra as follows

$$S(\lambda, v, z) = S_{\mathrm{a}}(\lambda, z)I(v, \sigma_v^{\mathrm{a}}) + S_{\mathrm{m}}(\lambda, z)I(v, \sigma_v^{\mathrm{m}}(T)), \tag{7}$$

TABLE 1. WMO OPTIMUM AND THRESHOLD REQUIREMENTS FOR WIND PROFILE MEASURE-MENT. SIMULATED ADM DOPPLER WIND LIDAR PERFORMANCES ARE CURSIVE AND BETWEEN BRACKETS. THE THRESHOLD REQUIREMENTS DENOTE THE MINIMUM REQUIREMENTS FOR EXPECTED POSITIVE IMPACT ON NWP. THE ADM-DWL MEETS ALL THRESHOLD REQUIRE-MENTS FOR COVERAGE AND ACCURACY IN THE PLANETARY BOUNDARY LOWER (PBL), TRO-POSPHERE (TROP.) AND STRATOSPHERE (STRAT.). TIMELINESS DENOTES THE MAXIMUM TIME THAT PASSES BETWEEN ANY OBSERVATION AND ITS DELIVERY TO THE USER. RELIABILITY DENOTES THE PROBABILITY THAT THE MEASUREMENT IS REPRESENTATIVE FOR THE ATMOS-PHERIC STATE.

		Optimum requirements			Threshold requirements		
		PBL	Trop.	Strat.	L.Trop.	H.Trop.	Strat.
vertical domain	(km)	0-2	2-16	16-30	0-5	5-16	16-26
vertical resolution	(km)	0.4 (1)	1 (1)	1 (1)	5	10	10
horizontal domain	(-)	global (80^oS-85^oN)			global		
horizontal integration	(km)	50 (50)			50		
number of profiles	(hour^{-1})	100000 (100)			100		
profile separation	(km)	50 (200)			500		
temporal sampling	(hour)	1 (12)			12		
timeliness	(hour)	1 (3)			4		
accuracy (component)	(m s^{-1})	1 (2)	1 (2-3)	1 (3)	5	5	5
error correlation	(-)	0 ($small$)			no number provided		
reliability	(%)	high (95)			high		

where $I(v, \sigma_v)$ denotes the normalised spectral distribution of the received signal in the wind velocity domain

$$I(v, \sigma_v) = \frac{1}{\sigma_v \sqrt{2\pi}} \exp\left(\frac{-(v - v_0)^2}{2\sigma_v^2}\right), \qquad (8)$$

with v_0 the mean wind velocity in the measurement cell and σ_v^a and σ_v^m the wind velocity standard deviations of the Mie and Rayleigh signal respectively, see Table 2. Figure 4 shows the typical shape of the spectral distribution of the atmospheric return signal as a superposition of the narrow aerosol (Mie) peak on top of the broad molecular (Rayleigh) peak. The centre of both peaks corresponds to the mean wind velocity in the measurement cell. The peak integrals $S_a(z)$ and $S_m(z)$ relate to the total energy of the return signal (in number of photons) from aerosol and molecular scattering respectively from an atmospheric layer at altitude z. They are quantified by (e.g. Winker 1996; Russel *et al.*1979)

$$S_x(\lambda, z) = \frac{E\lambda}{hc} \frac{\pi D^2}{4} \frac{\beta_x(\lambda, z)}{R(z)^2} \tau(\lambda, z)^2 \Delta z_{\text{LOS}} T_{\text{RX}} T_{\text{TX}}, \qquad (9)$$

where the subscript x denotes the type of scattering particle, i.e. a for aerosol and m for molecule. The number of scattering particles in the illuminated volume, $\beta(\lambda, z)$, and one-way atmospheric transmission, $\tau(\lambda, z)$, have been discussed in the previous section. Instrumental properties include laser energy E, the telescope diameter D, the range from the atmospheric layer to the instrument $R(z)$ and the depth of the illuminated layer, $\Delta z_{\text{LOS}} = \Delta z / \cos(\tilde{\phi})$, with Δz the range gate resolution and $\tilde{\phi}$ the line-of-sight or laser beam incidence angle. In the simulations we assume a uniform distribution of aerosols within a range gate. System optics are described with T_{TX} and T_{RX} that denote transmit and receive optics transmission respectively, c is the speed of light and h is Planck's constant, see Table 2.

(c) Earth radiance background

Besides backscattered light from atmospheric particles, part of the earth radiance is directed towards the telescope receiver. Daytime radiances have been computed using

LOWTRAN 7, based on the US Standard clear atmosphere, with multiple scattering, ground albedo 1 and sun local time between 10 and 12 am, see (e.g. Anderson *et al.*1995). The daytime earth radiance at 0.355μm then equals $L_{BKG} = 260$ W/(m^2 sr μm) and the corresponding number of photons at receiver input per micron equivalent bandwidth for one range gate equals

$$S_{BKG}(\lambda, z) = L_{BKG}(\lambda)\frac{\lambda}{hc}\frac{2\Delta z_{LOS}}{c}\left[\frac{\pi\Delta\theta_r D}{4}\right]^2 T_{RX}, \tag{10}$$

with $\Delta\theta_r$ the receiver field of view, see Table 2. The earth radiance causes a background signal whose spectrum is assumed uniform over the receiver bandwidth. The spectrum of the incoming signal thus constitutes the spectrum displayed in Fig. 4 on top of a uniform broad spectrum.

(d)   *Signal detection and processing*

Backscattered light from atmospheric particles is collected by the telescope and directed to the instrument receiver. Detection of the backscattered signal is based on incoherent (or direct) detection techniques involving high resolution spectrometers (interferometers), (e.g. Abreu 1979). The receiver samples the signal in the time domain in order to determine its arrival time and hence the distance to the atmospheric layer. Signals falling within a range gate are accumulated. For each range gate, a spectral filter extracts the central part of the spectrum and directs it towards the Mie multi-channel receiver for further processing. The spectrum of the remaining signal mainly shows the slopes of the broad Rayleigh signal and is processed by a double-edge technique, named Rayleigh dual-channel.

i   *Mie multi-channel receiver* The spectrum of the signal arriving at the Mie receiver typically shows a narrow peak on top of a broadband spectrum, the latter corresponding to the molecular and earth emitted radiance signal. The receiver bandwidth is 225 m s^{-1} and subdivided into 16 bins, providing a sampling resolution of about 14 m s^{-1}. The signal is sampled with a fringe imaging technique based on a Fizeau interferometer and CCD detection (Morançais 2002; ESA 1999). The interferometer spectral transmission is assumed Lorentzian shaped with a resolution compatible with the sampling resolution, i.e. with a full width at half-maximum (FWHM) of 4.62×10^{-14} meter which corresponds to about 20 m s^{-1} at 0.355μm laser wavelength. As a result, the narrow peak of the incoming signal is dispersed on a few bins. The total number of generated charges after accumulation on the detector from aerosol (Mie) scattering per range gate equals

$$N_{Mie}(\lambda, z) = \eta N_s S_a(\lambda, z)T_p\frac{1}{N}\frac{\Delta\lambda_{fizeau}}{\Delta\lambda_{USR}} \tag{11}$$

with η the detector quantum efficiency, N_s the number of accumulated shots, i.e. typically 700 for ADM, see section 5, T_p the peak transmission of the complete receiver and $\Delta\lambda_{fizeau}$ and $\Delta\lambda_{USR}$ the Fizeau interferometer resolution and useful spectral range respectively, see Table 2. The average spectral response of channel i depends on the wind velocity in the measurement cell and is computed through the convolution of the interferometer spectral transmission response function and the normalised spectral distribution of the received signal, Eq. (8).

The received Mie signal is contaminated with noise from molecular (Rayleigh) scattering and the earth radiance. To allow for operation in daylight conditions this noise is reduced through a train of spectral blocking filters consisting of Fabry-Perot

interferometers (ESA 1999). The effect of the blocking train is approximated by an equivalent square filter at detector input with an equivalent bandwidth of $\Delta\lambda_{\text{eq\_Ray}}$ for the Rayleigh signal and $\Delta\lambda_{\text{eq\_BKG}}$ for the earth radiance, see Table 2. The total number of charges due to Rayleigh scattering that are detected after accumulation is modelled through

$$N_{\text{B\_Ray}}(\lambda, z) = 2\eta N_s S_{\text{m}}(\lambda, z)\left[\frac{\Delta\lambda_{\text{eq\_Ray}} + \Delta\lambda}{\Delta\lambda_{\text{FWHM\_Ray}}}\right]\sqrt{\frac{\ln(2)}{\pi}}T_p\frac{2}{\pi}, \qquad (12)$$

with

$$\Delta\lambda_{\text{FWHM\_Ray}} = \frac{2\lambda}{c}\sqrt{\frac{8\ln(2)k_{\text{B}}T}{(M_{\text{air}}/N_{\text{avo}})}}, \qquad (13)$$

the FWHM of the Rayleigh signal spectral shape for temperature T and with M_{air} the air molecular weight, k_{B} Boltzmann constant and N_{avo} Avogadro number, see Table 2. For the number of charges due to the earth radiance background after accumulation we have

$$N_{\text{B\_BKG}}(\lambda, z) = \eta N_s S_{\text{BKG}}(\lambda, z)T_p\Delta\lambda_{\text{eq\_BKG}}\frac{2}{\pi} \qquad (14)$$

Since, we assume the spectral distributions from Rayleigh scattering and the earth radiance uniform in the useful spectral range, their respective generated charges are equally distributed over the 16 spectral channels.

Generated charges are collected on an accumulated CCD device that is build up of 16 channels or bins. The signal registered on each bin is contaminated with noise from five contributors, i.e. noise due to dark charges, $N_{\text{DC}} = 0.95$ electrons RMS, the CCD read-out stage, the pre-amplifier unit, the digitisation chain and digitisation noise, from which noise at the CCD read-out stage is most significant with a value of 3 electrons RMS. Noise contributors are assumed independent giving a total noise, N_{noise}, of about 3.52 electron RMS per bin after accumulation. Since counting processes are described by Poisson distributions, the standard deviation of noise equals the square root of the number of detected events and since the number of detected photons is sufficiently high, we approximate noise with a Gaussian noise process. Hence, the number of detected photons at altitude z on bin i has been simulated by

$$\tilde{N}_{\text{tot}}(z, i) = N_{\text{tot}}(z, i) + N_{\text{DC}} + G(0, 1)\sqrt{N_{\text{tot}}(z, i) + N_{\text{noise}}^2} \qquad (15)$$

$$N_{\text{tot}}(z, i) = N_{\text{Mie}}(\lambda, z)R_{\text{Fiz}}(i) + N_{\text{B\_Ray}}(\lambda, z)/N + N_{\text{B\_BKG}}(\lambda, z)/N, \quad (16)$$

with $G(0, 1)$ the standard normal Gaussian distribution with zero mean and standard deviation 1, R_{Fiz} the fraction of total detected Mie photons falling in bin i and N the number of channels of the receiver.

A typical example at 1.5 km above mean sea level gives $\beta_{\text{a}} = 1.46\times10^{-6}$ m^{-1}sr^{-1}, $\beta_{\text{m}} = 6.59\times10^{-6}$ m^{-1}sr^{-1} and $\tau = 0.53$ from Fig. 2. The corresponding atmosphere return signal from a single shot collected by the telescope then gives $S_{\text{a}} = 366$, $S_{\text{m}} = 1651$ and $S_{\text{BKG}} = 5.1393\times10^5$ from Eqs. (9, 10). The accumulated signal measured by the CCD detector from Mie scattering, Rayleigh scattering and the earth radiance after filtering then equals $N_{\text{Mie}} = 4710$, $N_{\text{B\_Ray}} = 7095$ and $N_{\text{B\_BKG}} = 221$ from Eqs. (11, 12, 14). These numbers show that even in daylight conditions, the MIE receiver is not very sensitive to the earth radiance. Figure 4 shows a typical realisation of the detected signal on the Mie multi-channel receiver from Eqs. (15, 16) for a zero mean wind velocity in the measurement cell. A centroid computation over the 16 bins provides the location
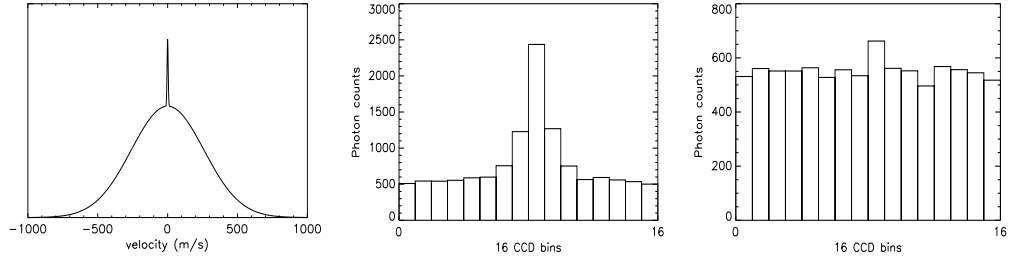
Figure 4.   Typical spectral shape in the wind velocity domain of the detected signal on the telescope receiver for zero wind velocity in the measurement volume. Left, theoretical noise-free shape from Eq. (7). The narrow/broad peak corresponds to detected laser light backscattered from atmospheric aerosols/molecules. Typical shape of noisy spectra measured with the Mie multi-channel receiver at 1.5 km altitude (middle) and 10.5 km altitude (right) from mean sea level. The receiver bandwidth of 225 m s^{-1} is subdivided in 16 bins, each representing a range of 14 m s^{-1}. This enables HLOS wind measurements between -110 and 110 m s^{-1}.
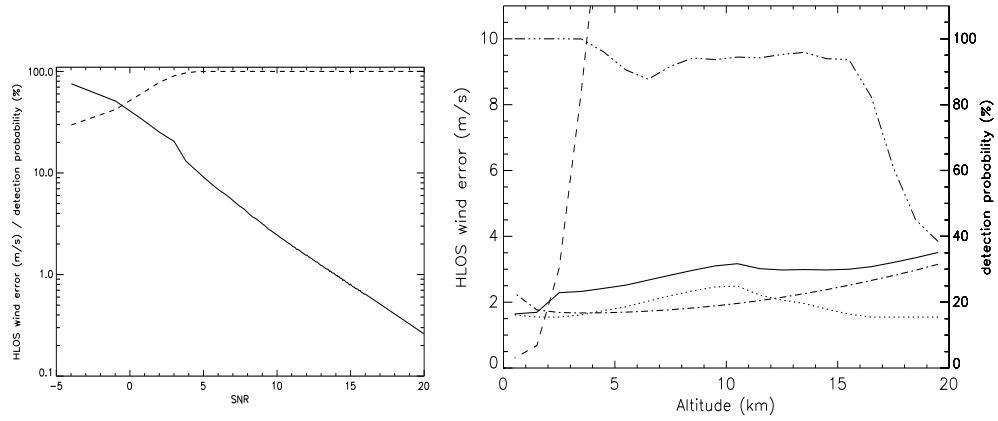

Figure 5.   Space-borne DWL performance in non-cloudy conditions. Left, HLOS wind RMS error (solid) and detection probability (dashed) as a function of SNR for the MIE multi-channel receiver. Right, corresponding standard deviation of the HLOS wind error estimate (dashed) and detection probability (dash-dot-dot-dot) as a function of altitude. In addition the HLOS wind error as obtained from the Rayleigh dual-channel (dash-dot), a representativeness error for sampling along a horizontal line of 50 km (dot) and the total observation error (solid) are displayed.

of the spectrum centre and thus of the Doppler shifted frequency. Rayleigh scattering and background radiance generated signals act as noise that could result in bad peak detections. To minimize noise influence three contiguous bins are added. The noise background level is estimated and defi nes a threshold value. If none of the accumulated bin values exceeds the threshold, the acquisition is declared as a non-detection, i.e. no Mie peak is provided. Otherwise, a wind estimate is determined by

$$v_{\text{LOS}}(z) = \frac{v_{\text{range}}}{16} \left[\frac{\sum_{k=i_{\max}-2}^{i_{\max}+2} k \tilde{N}_{\text{tot}}(z, k)}{\sum_{k=i_{\max}-2}^{i_{\max}+2} \tilde{N}_{\text{tot}}(z, k)} - 9 \right], \qquad (17)$$

with v_{range} the spectral bandwidth of the receiver, i.e. 225 m s^{-1}, $i_{\max}$ denotes the bin with maximum value and the value 9 denotes the central bin and corresponds to zero wind velocity. For a large number of realisations we determined the detection probability

and wind RMS error estimate, σ_v^{Mie}, as a function of SNR in a Monte Carlo study, based on Eqs. (15,16,17). Here, SNR is defined through

$$\text{SNR} = 10 \log \left[\frac{N_{\text{Mie}}}{\sqrt{N_{\text{Mie}} + N_{\text{B\_Ray}} + N_{\text{B\_BKG}} + N \times N_{\text{Noise}}^2}} \right] \qquad (18)$$

Next, this result is used the determine the performance of the Mie channel as a function of altitude. For the typical example at 1.5 km we have an SNR of 16.3, corresponding to a detection probability of 1 and HLOS wind RMS error of about 0.7 m s^{-1}. These results are summarized in Fig. 5 and show that the Mie multi-channel receiver provides good wind estimates in the lower atmosphere only up to two kilometer altitude. Note that the performance of the Mie channel decreases for low aerosol backscatter regimes. This is not critical for Aeolus since low aerosol concentrations implies low signal attenuation from aerosol scattering and absorption, resulting in a better performance of molecular backscatter retrieved winds by the Rayleigh dual channel as discussed in the next section.

ii   *Rayleigh dual channel receiver* The Rayleigh dual-channel receiver technique is an edge technique to measure the slopes of the Rayleigh spectrum, see Fig. 4. Two Fabry-Perot interferometers are positioned roughly symmetrically around the centre wavelength position of the Rayleigh peak in order to perform a differential measurement. Modelling of collected signals on both channels is similar as for the Mie multi-channel technique Eqs. (12,14)

$$N_{\text{FP}}(\lambda, z, i) = \frac{1}{2} \eta N_s S_{\text{m}}(\lambda, z) T_p R_{\text{FP}}(i), \qquad i = 1, 2, \qquad (19)$$

with $R_{\text{FP}}(i)$ the spectral response of filter i that is a convolution of the interferometer spectral transmission response function and the normalised spectral distribution of the received signal, Eq. (8), see also Table 2. For the background it is assumed that both channels are illuminated with the same level of earth radiance with values of

$$N'_{\text{B\_BKG}}(\lambda, z, 1) = N'_{\text{B\_BKG}}(\lambda, z, 2) = \frac{1}{2} \eta N_s S_{\text{BKG}}(\lambda, z) T_p \Delta\lambda'_{\text{eq\_BKG}} \qquad (20)$$

where $\Delta\lambda'_{\text{eq\_BKG}}$ differs from $\Delta\lambda_{\text{eq\_BKG}}$ in Eq. (14), see Table 2.

In order to limit as far as possible the read-out noise, the first (channel 1) and last (channel 2) 8 bins are accumulated before read-out, giving a total noise of $N'_{\text{noise}} = 4.19$ electron RMS per channel after accumulation. For the noisy signals on both channels we may then write

$$\tilde{N}'_{\text{tot}}(z, 1) = \sum_{i=1}^{8} (N'_{\text{tot}}(z, i) + N_{\text{DC}}) + G(0, 1) \sqrt{\sum_{i=1}^{8} N'_{\text{tot}}(z, i) + N'^2_{\text{noise}}} \quad (21)$$

$$\tilde{N}'_{\text{tot}}(z, 2) = \sum_{i=9}^{16} (N'_{\text{tot}}(z, i) + N_{\text{DC}}) + G(0, 1) \sqrt{\sum_{i=9}^{16} N'_{\text{tot}}(z, i) + N'^2_{\text{noise}}} \quad (22)$$

$$N'_{\text{tot}}(z, i) = N_{\text{FP}}(\lambda, z, i) + N'_{\text{B\_BKG}}(\lambda, z, i) \quad i = 1, 2 \qquad (23)$$

The difference between detected photon counts at each channel corresponds to the Doppler shifted wavelength position and thus the LOS wind component as follows

$$v_{\text{LOS}}(z) = \left[\frac{\tilde{N}'_{\text{tot}}(z, 1)}{\tilde{N}'_{\text{tot}}(z, 2)} - 1 \right] \left(\frac{\partial R}{\partial v} \right)^{-1}, \qquad (24)$$

with $\partial R / \partial v$ the receiver sensitivity, see Table 2.

The earth radiance background acts as noise and potentially results in biases of the frequency estimate. The choice of orbit and viewing angle, i.e. towards the dark part of the earth in combination with spectral blocking filters minimizes this effect. For the system parameters in Table 2, the bias is about 1.5% in the lower troposphere and equals about 4% at 20 kilometer. These values are too high to be ignored and could be detrimental for assimilation in NWP models (Stoffelen *et al.*2002). However, in the remainder we ignore wind biases and anticipate on the possibility to estimate the earth radiance background and subtract it before processing or to reduce its contribution by spectral filters to below the threshold of 0.5%. The standard deviation of error, $\sigma_v^{\text{Ray}}(z)$, of estimated HLOS wind estimates using this technique is a function of altitude and estimated by

$$\sigma_v^{\text{Ray}}(z) = \frac{1}{\text{SNR}_{\text{DC}}(z)} \left(\frac{\partial R}{\partial v} \right)^{-1} \frac{1}{\sin(\tilde{\phi})}, \tag{25}$$

with

$$\text{SNR}_{\text{DC}}(z) = \frac{N_{\text{FP}}(z,1) + N_{\text{FP}}(z,2)}{\sqrt{\tilde{N}'_{\text{tot}}(z,1) + \tilde{N}'_{\text{tot}}(z,2)}} \tag{26}$$

A typical example at 1.5 km gives $N_{\text{FP}}(\lambda, 1500, 1) = N_{\text{FP}}(\lambda, 1500, 2) = 34812$ from Eq. (19) and $N'_{\text{B\_BKG}}(\lambda, z, 1) = N'_{\text{B\_BKG}}(\lambda, z, 2) = 3096$ from Eq. (20). Then, $\tilde{N}'_{\text{tot}}(z, i)$ equals 37909 on average. Substituting in Eq. (25) gives $\sigma_v^{\text{Ray}}(1500) = 1.75$ m s^{-1}. The Rayleigh dual channel performance curve is displayed in the right figure of Fig. 5. Note that detection probability equals 1 for the Rayleigh dual-channel receiver, since a wind estimate is retrieved in all cases. To arrive at the total measurement error, σ_{tot}, we add a representativeness error, σ_{r}, to the instrument error, σ_v, that accounts for wind variability in the target volume and the corresponding error of measuring only part of that volume (Lorenc *et al.*1992). For the total measurement error displayed in Fig. 5 we have

$$\sigma_{\text{tot}}(z) = \sqrt{\left\{ \text{MIN}\left[\sigma_v^{\text{Mie}}(z), \sigma_v^{\text{Ray}}(z) \right] \right\}^2 + \sigma_{\text{r}}^2} \tag{27}$$

From Fig. 5 we note that the accuracy of HLOS wind measurements meets the WMO requirements, as stated in Table 1, in cloud-free atmospheres up to 16 km altitude. Reducing the vertical resolution to 2 km at higher altitudes would meet the accuracy requirement up to 20 km. The aerosol channel provides wind measurements up to 2 km altitude and the molecular channel up to 20 km or higher. No advanced processing scheme is considered here to simultaneously exploit the information content of both channels, which could increase performance most notably in the middle troposphere in the presence of more than average aerosol concentrations. Systematic errors are expected to be much smaller than variable (random) errors and ignored here in the simulation of HLOS winds.

5.　ADM SAMPLING AND CLOUDS

Cloud is one of the crucial parameters for the wind measurement capability of a space-borne DWL. About 70% of the earth surface is covered by clouds. Cloud tops return a large signal to the lidar detector, yielding high-quality wind estimates in principle, but they may not be representative for the ambient flow e.g. due to internal cloud dynamics. This is true particularly in meteorologically unstable conditions, such

TABLE 2.   MAIN CHARACTERISTICS OF THE ESA ATMOSPHERIC DYNAMICS MISSION CONCEPT THAT IN-
CLUDES A DOPPLER WIND LIDAR MOUNTED ON A POLAR ORBITING SATELLITE. PARAMETERS SPECIFICALLY
NAMED ARE FOUND IN THE TEXT.

ADM	parameter	description	value	unit
Orbit	-	satellite altitude	400	km
	-	satellite velocity	7	km s^{-1}
	-	inclination angle	97.2	degrees
	ϕ	laser off-nadir angle	35	degrees
	$\tilde{\phi}$	earth surface incidence angle	37.56	degrees
	ψ	LOS azimuth angle (w.r.t. subsatellite track)	90	degrees
	Δz	range gate resolution	1000	m
	-	duty cycle	25	%
Emitter laser	λ	wavelength	0.355	μm
	E	laser pulse energy	0.13	J
	-	linewidth FWHM	25	MHz
	PRF	pulse repetition frequency	100	Hz
Optics	T_{TX}	transmit optics transmission	0.9	-
	T_{RX}	receive optics transmission	0.9	-
	D	telescope diameter	1.1	m
	$\Delta\theta_r$	receiver field of view	3.5×10^{-4}	radians
Blocking filters	-	interference filter FWHM	5	nm
	-	interference filter peak transmission	0.9	-
	T_p	peak transmission MIE/Rayleigh receiver	0.3/0.45	-
	$\Delta\lambda_{\text{eq\_Ray}}$	equiv. bandw. for Mie receiver on Rayleigh	0.044	pm
	$\Delta\lambda_{\text{eq\_BKG}}$	idem for Mie receiver on earth radiance	4.3	pm
	$\Delta\lambda'_{\text{eq\_BKG}}$	idem for Rayleigh receiver on earth radiance	50	pm
	-	medium resolution filter FWHM	1	pm
	-	medium resolution filter peak transmission	0.7	-
Mie high resolution filter (Fizeau)	$\Delta\lambda_{\text{fizeau}}$	Fizeau spectral width at FWHM	0.044	pm
	$\Delta\lambda_{\text{USR}}$	useful spectral range	0.53	pm
	$\Delta\lambda$	spectral sampling	0.033	pm
	σ_v^{a}	standard deviation of Mie spectrum	4	m s^{-1}
Rayleigh filters (Fabry-Perot)	$\partial R/\partial v$	receiver sensitivity	3.7×10^{-3}	(m s^{-1})$^{-1}$
	$\sigma_v^{\text{m}}(T)$	standard deviation of Rayleigh spectrum	277	m s^{-1}
Accumulation CCD	η	quantum efficiency	0.75	e- ph^{-1}
	-	number of accumulations per observation	14	-
	-	number of shots per accumulation	50	-
	N_s	number of accumulated shots (49 km)	700	-
	N	number of channels (bins)	16	-
physical constants	c	speed of light	3×10^{8}	m s^{-1}
	h	Planck's constant	6.62×10^{-34}	J s
	k_{B}	Boltzmann constant	1.38×10^{-23}	JK^{-1}
	N_{avo}	Avogadro number	6×10^{23}	mol^{-1}
	M_{air}	air molecular weight	29×10^{-3}	kg mol^{-1}

as convection in the tropics where the vertical wind component may not be neglected. Moreover, optically thick clouds obscure the underlying atmosphere and thus prevent the laser beam to penetrate deep into the atmosphere. Nevertheless, a number of shots might still reach the lower atmosphere and provide a wind retrieval in cases of broken cloud and for optically thin clouds, depending on cloud cover and cloud liquid/ice-water content. In such heterogeneous conditions it is important that the 7 seconds laser active period is subdivided in 14 equidistant periods, the so-called accumulation periods. During 0.5 seconds i.e. for 50 laser pulses, corresponding to about 3.5 km along track, the return signal from the atmosphere is accumulated on the instrument receiver for SNR

enhancement. Next, the 14 accumulated signals are processed simultaneously to exploit their information content in an optimal way. For cloud-free atmospheres processing may be straightforward by adding the spectra of all accumulations and retrieving a single HLOS wind profile according to Eqs. (3, 17, 24). For cloudy atmospheres quality control becomes important and a more advanced processing scheme is required that discriminates between cloud and aerosol returns e.g. based on signal strength and variability in both the Mie and Rayleigh receiving channels.

To simulate the ADM sampling in cloudy atmospheres we used realistic atmospheric conditions extracted from the nature run database at ECMWF (Becker *et al.*1996), i.e. for the period 5 February 1993 until 7 March 1993. For each location of lidar-measured winds cloud coverage and cloud liquid-water are extracted from the database. Cloud encounter is determined by the cloud coverage in the measurement cell and a random number generator. The cloud scene is assumed fixed during accumulation, implying that within 3.5 km all or none of the shots at a particular vertical level encounter cloud. This can be motivated by the fact that generally the cloud cover variability over 3.5 km is much smaller than the cloud cover variability on scales between 3.5 and 50 km. Cloud variability is defined as $\int E(k)\mathrm{d}k$, with $E(k)$ the wave number density spectrum and k denoting wave number, i.e. the inverse of the length scale (Feijt *et al.*2000). For instance, assuming $E(k) \propto k^{-5/3}$ the ratio of these variabilities equals 0.2.

If cloud coverage is reported in adjacent vertical levels we assume a single cloud that extends over several vertical layers. In these cases the ECMWF cloud overlap model is applied that assumes maximum overlap between clouds at adjacent levels (Tiedtke 1993). In scenes of broken clouds some of the accumulations correspond to cloud returns while others to aerosol returns. We assume cloud top returns representative for the ambient flow. This assumption is valid for most and in particular stratiform clouds, but is too optimistic for convective (broken) clouds, most frequent in the tropics, because of cloud dynamics. Areas with anomalously strong vertical motion are usually covered by optically thick cloud and not visible by a space-borne DWL. Moreover, the segregated shot accumulations guarantee returns from aerosol or molecules besides the dynamically active cloud top returns within a cluster of integration. Careful treatment and quality control of these accumulations might still produce a representative estimate of the flow at these scenes or in cases of extreme backscatter or wind variability result in rejection at certain levels. Effects of multiple scattering are neglected due to the small laser beam footprint size of 7 meter diameter.

Inside each range gate we assumed a homogeneous distribution of aerosol particles. This assumption may not be valid in cases of aerosol stratification, e.g. due to strong vertical wind-shear and aerosol plumes, e.g. from advected Saharan dust. The lidar-in-space-technology experiment (LITE) shows some clear examples (Winker 1996). For these situations and also for optically thin clouds the assignment of the wind measurement to the centre of the range gate may be incorrect. Height assignment errors up to half the range gate resolution of 1 kilometer could have a detrimental impact in data assimilation systems (Stoffelen *et al.*2002), but are ignored here motivated by the prospect that advanced quality control schemes will detect such cases and handle retrieved winds in an appropriate manner, not destroying NWP analyses. We take into account large spatial variability of aerosol particles. For each measurement, separated by 200 kilometer, we simulated an aerosol backscatter profile from the aerosol backscatter statistics of Fig. 2 and a normal-distributed random-number generator (Marseille and Stoffelen 1998). Although aerosol variability may be large in the vertical it is generally

TABLE 3. PERCENTAGE OF CLOUD-FREE AIR SCENES BY GEOGRAPHICAL AREA OF THE ATMOSPHERIC
DATABASE THAT IS USED IN THE SIMULATION OF THE ADM DWL (FEBRUARY 1993).

Region	Polar	Storm	Subtrp.	Tropics	Subtrp.	Storm	Polar
Latitude	$>60^\circ$S	60°S-40°S	40°S-20°S	20°S-20°N	20°N-40°N	40°N-60°N	$>60^\circ$N
cloud-free (%)	37	27	32	18	40	31	34

well distributed over a distance of 50 kilometer (Marseille *et al.* 2002). Hence, we assumed aerosol backscatter constant over 50 kilometer intervals.

The ECMWF OSSE database (Becker *et al.* 1996) has been extended with simulated Doppler wind lidar data according to the described ADM concept. HLOS wind profiles have been determined for the complete nature run time period from 5 February 1993 until 7 March 1993. Each profile contains HLOS winds that are composed of the true HLOS wind, according to Eq. (2), and a measurement error as computed from the standard deviation of error, Eq. (27), and a Gaussian-distributed random-number generator. No correlations between errors have been assumed. This is motivated by the fact that Aeolus is designed to be a very stable system (ESA 1999) and systematic errors are subtracted in NWP of observation use. Moreover we anticipate on advanced quality control schemes to optimise the use of retrieved winds with correlated error structures in NWP models (Stoffelen *et al.* 2002).

We considered the effect of convective clouds in the upper troposphere that could potentially provide an effective reflection cross section of sunlight in the direction of the receiver, thereby anomalously increasing the background radiation, hence introducing large biases in the retrieved winds. From inspection of the intensities as observed on METEOSAT visible images, we however concluded that this condition is relatively rare and associated with extreme spatial variability in background radiation, and probably detectable by straightforward quality control in an integration area. As such no concern about substantial biases remains and biases are ignored in the simulation of HLOS wind profiles.

A statistical analysis of the ADM-DWL OSSE database data has been performed to assess cloud impact on data quality. The percentage of cloud-free scenes in Table 3 indeed confirms an average coverage of the earth surface by about 70%, with a maximum of 82% in the tropics. These values have to be interpreted carefully since cloud porosity permits wind retrieval below clouds in many cases as confirmed by LITE and cloudy scenes often consist of broken clouds that permit wind retrieval when using the ADM multiple-shot sampling strategy.

Four classes of data quality have been defined ranging from high, good, low to very low quality. The measurement error as defined in Eq.(27) is inherently a function of altitude, irrespective of the proposed lidar instrument, due to the presence of a representativeness error. Measurement errors of conventional wind profiling instruments such as radiosondes include a representativeness error for point measurements, hereafter denoted $\sigma_{rp}(z)$. From these considerations we decided to classify HLOS wind errors relative to point measurement representativeness error and as a function of altitude as follows: high quality for $\sigma_{tot}(z) < \sigma_{rp}(z)$, i.e. better than radiosondes, good quality for $\sigma_{rp}(z) \leqslant \sigma_{tot}(z) < 2\sigma_{rp}(z)$, low quality for $2\sigma_{rp}(z) \leqslant \sigma_{tot}(z) < 3\sigma_{rp}(z)$ and very low quality for $\sigma_{tot}(z) \geqslant 3\sigma_{rp}(z)$. Since HLOS winds are retrieved from an accumulation along a line of 50 kilometer, its representativeness error is smaller than for point measurements. We assumed that a reduction of 20% of error variance is obtained, resulting in $\sigma_r(z) = 0.89\sigma_{rp}(z)$ as depicted in Fig. 5. The classification permits high quality wind measurements from the Mie channel in the lower atmosphere and regions
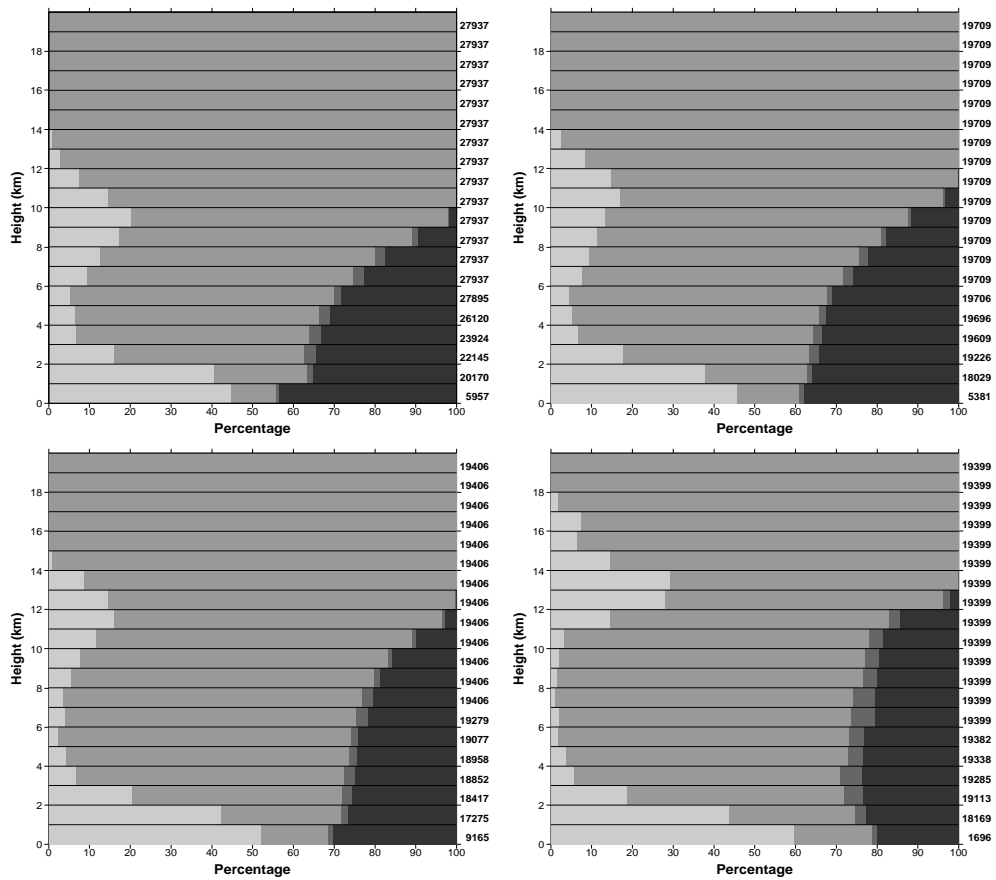
Figure 6. ADM Aeolus performance in four global regions i.e. the northern and southern hemisphere polar region above 60 degrees latitude (upper left), the storm track regions between 40 and 60 degrees latitude (upper right), the subtropics between 20 and 40 degrees latitude (lower left) and the tropics between 0 and 20 degrees latitude on northern and southern hemisphere (lower right). Gray-scale values from bright to dark denote high, good, low and very low quality HLOS wind data. The numbers on the right-hand side of the figures denote the number of data on which statistics are based. Less data are available close to the surface due to orography.

of large concentrations of scattering particles such as cloud and aerosol stratification in the mid-troposphere. Figure 6 displays HLOS wind quality as a function of altitude for four global regions. In cloud-free conditions, high-quality data are expected mainly in the lower troposphere up to 3 kilometer and occasionally at higher altitudes for high aerosol density. The Rayleigh channel provides good quality HLOS winds above 3 kilometer up to 20 kilometer altitude. Low and very low quality data occur in the mid-troposphere due to cloud obstruction. Figure 6 confirms the cloud penetrating ability of Aeolus and shows wind retrievals close to the earth surface below clouds due to the strong aerosol signal in the PBL. The presence of cloud is most critical around the tropopause and cloud cover in the tropics is most extensive. It is interesting to note that the apparently optically thin clouds in the tropics above 14 kilometer altitude do not completely obscure the underlying atmosphere and still enable good quality data from below. The cloud penetrating capability of optically thin (e.g. cirrus) clouds by a lidar was already observed with LITE (Winker et al.1997). Cloud obstruction is relatively constant in the tropics since high-level clouds tend to overlap with lower-level clouds

below the tropopause level. The obstruction of 25% indicated by the dark and black bars in Fig. 6 show that in about 75% of cases a complete wind profile is obtained. Note that the choice of classification implies that bright bars in Fig. 6 denote winds of better quality than radiosonde and originate either from scenes of high aerosol concentrations or clouds. The slightly darker gray-scale bars correspond mainly to Rayleigh retrieved winds and the choice of classification implies that their quality is somewhere between slightly better than radiosonde and slightly worse than radiosonde depending on altitude. This means that about 75% of DWL HLOS winds is close to radiosonde quality or better. This would result in about 100 profiles per hour classified here as good quality or very good, hence fulfilling the WMO minimum requirement on coverage, see Table 1.

Figure 7 displays the geographical distribution of quality for lidar-measured HLOS winds. To arrive at these figures, the globe has been subdivided in pixels of 2 degrees latitude by 2 degrees longitude. The quality of HLOS winds in the period from 6 February until 20 February 1993 falling within a pixel have been averaged and displayed with the same gray scale classification as in Fig. 6. Thus, bright spots indicate high quality winds while dark spots indicate low quality winds. White spots denote data void locations. At 200 mb HLOS wind data are generally retrieved from molecular scattering with the Rayleigh dual channel and of good quality. High quality winds correspond to cloud returns and are mainly found in the storm track regions. Low quality winds are due to obstruction from clouds aloft and are mainly found in the tropics. Obviously, there is strong correlation between low quality spots at 200 and 500 mb due to clouds aloft. Going downwards into the atmosphere the number of high quality spots increases at 850 and 1000 mb because of an increasing aerosol density, enabling HLOS wind retrieval from the Mie channel. From Figs. 6 and 7 it is clear that the mid-troposphere around 500 mb seems to suffer most from clouds. For instance zooming in on the northern Atlantic in Fig. 7 shows many clouds around 200 mb, obscuring the underlying atmosphere, hence reducing wind quality at 500 mb. This might be a prelude of expected moderate lidar impact on NWP analysis in the northern Atlantic and short-term forecasts over Europe in impact assessment experiments (OSSE).

6. SUMMARY AND CONCLUSIONS

The European Space Agency (ESA) has decided to fly a Doppler wind lidar on a polar orbiting satellite platform in 2007 in the context of the Aeolus mission. The performance of Aeolus has been simulated for cloud-free and cloudy conditions. The lidar concept has evolved over the years and the ADM objective is now to demonstrate improvements in meteorological analyses by the use of space-borne DWL wind profiles. Aeolus measures profiles of single horizontal line-of-sight wind components with a vertical resolution of 1 km ranging from the earth surface up to at least 20 km altitude. The proposed lidar operates in the ultraviolet part of the electromagnetic spectrum at $0.355\ \mu$m laser wavelength. This enables wind retrieval from Doppler shifted frequencies induced by moving atmospheric aerosols and molecules. The received atmospheric signal on the collecting telescope area is split and processed by two separate channels to enable wind retrieval from aerosol (Mie) and molecular (Rayleigh) scattering independently. Advanced CCD detectors enable the accumulation of received signals from several subsequent pulses hence minimizing detection noise. This design makes Aeolus a powerful concept since it relaxes requirements on instrument sizing. In low aerosol regimes the Rayleigh channel provides good quality (comparable to radiosonde) winds in general, while in high aerosol regimes the Mie channel takes over.
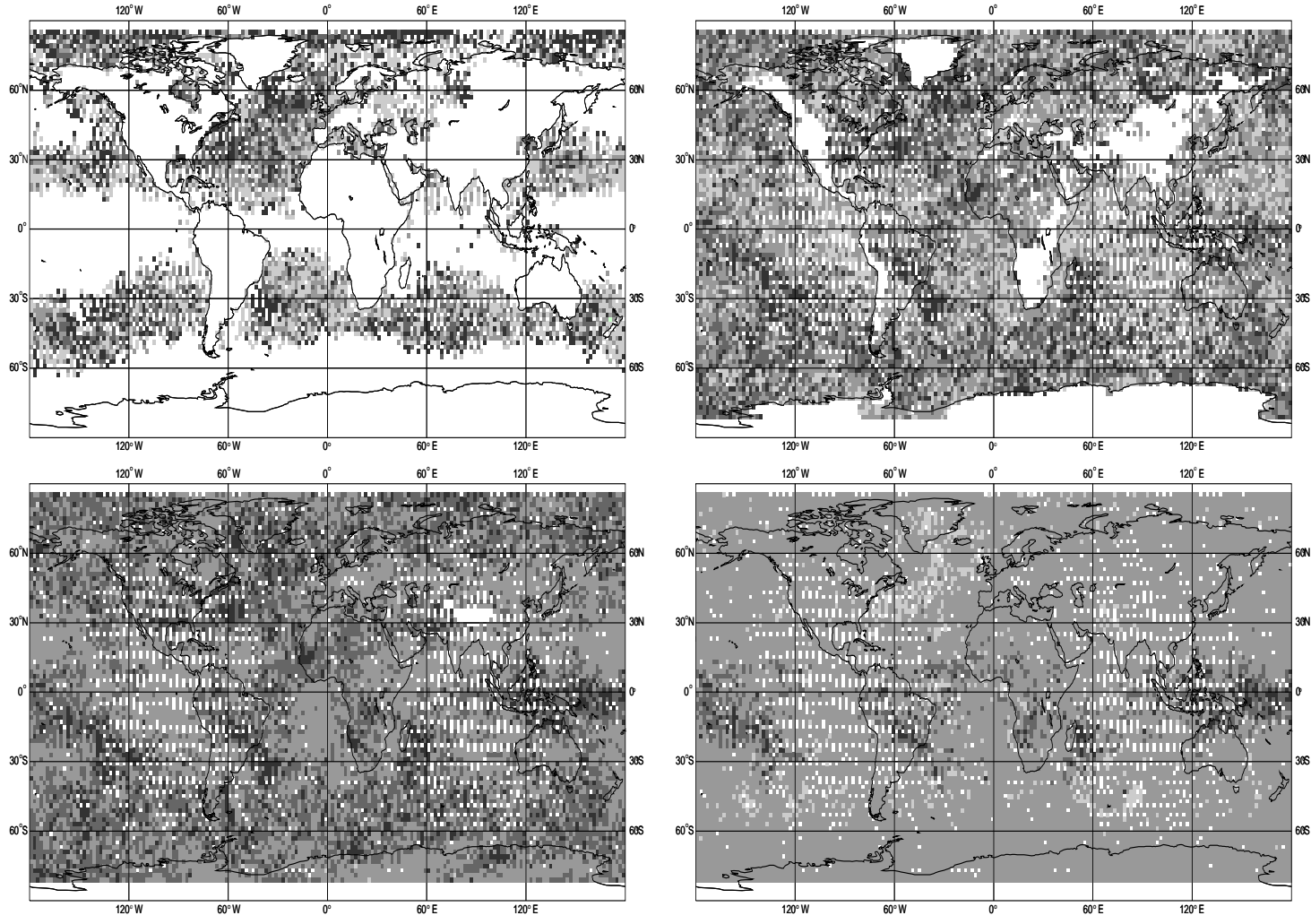
Figure 7. Geographic distribution of lidar data quality over the period 6 February 1993 until 20 February 1993 for four pressure levels: 1000 mb (upper right), 850 mb (lower right), 500 mb (upper left) and 200 mb (lower left). White spots denote data void locations due to orbit coverage or surface pressure level. Gray scales are similar as in Fig. 6.

Atmospheric conditions, such as the global distribution of aerosols and clouds play a key role in the expected quality of retrieved wind profiles. Realistic atmospheric conditions were obtained from a Global Circulation Model (GCM) and climatological databases of aerosol distribution. The simulated lidar measured wind profiles meet the optimum WMO quality requirement and minimum coverage requirements in clear air. In the storm track region and tropics we found only a 25% coverage reduction in the lower troposphere due to clouds aloft. The height resolution of 1 km, a small footprint and multiple shot capability are the main reasons for this.

The existing OSSE database of simulated meteorological observations at ECMWF has been extended with simulated DWL horizontal line-of-sight wind profiles according to the ADM concept. This enables assessment of their potential impact on numerical weather prediction and climate processes by so-called observation system simulation experiments (OSSE).

In the simulations of horizontal line-of-sight wind profiles and their uncertainty we did not take into account measurement biases. These may be induced by several sources of system imperfections and/or heterogeneous atmospheric conditions (Stoffelen *et al.* 2002; Marseille *et al.* 2002). In extreme cases such as convective clouds in the upper troposphere that are in the receiver field of view or when observing over regions with large surface albedo (arctic ice), the background signal may introduce large biases for wind retrieval from the Rayleigh dual channel receiver. Besides biases, correlated error structures between or within measured wind profiles may be detrimental when assimilated in NWP models (Stoffelen 2002). Such structures may be due to e.g. aerosol layers that extend over hundreds of kilometers and induce height assignment errors in subsequent wind profiles. To limit the effect of system imperfections, Aeolus must be designed to be a stable system such that systematic errors are constant over time and can easily be removed by NWP models. In addition advanced quality control schemes need to be developed to detect extremely variable atmospheric scenes and apply adequate processing to minimise measurement biases and correlated error structures.

7. Acknowledgment

References

Abreu, V. J.	1979	Wind measurements from an orbital platform using a lidar system with incoherent detection: an analysis *Appl. Opt.* **18,** *No 17, 2992–2997*
Anderson, G. P., Kneizys, F. X., Chetwynd, J. H., Wang, J., Hoke, M. L., Rothman, L. S., Kimbal, L. M., McClatchey, R. A.	1995	FASCODE/MODTRAN/LOWTRAN *18th Annual Review Conference on Atmospheric Transmission Model*
Baker, W. E., and Co-authors	1995	Lidar-measured winds from space: a key component for weather and climate prediction. *Bull. Am. Meteorol. Soc.,* **76,** *869–888*
Becker, B. D., Roquet, H., Stoffelen, A.	1996	A simulated future atmospheric observation database including ATOVS, ASCAT, and DWL. *Bull. Am. Meteorol. Soc.,* **77,** *2279–2294*
European Space Agency	1996	The Nine Candidate Earth Explorer Missions-Atmospheric Dynamics Mission. *ESA SP-1196(4)*

European Space Agency   1999   Atmospheric Dynamics Mission. The four candidate earth ex-
                                          plorer missions. Report for mission selection. *ESA SP-
                                          1233(4)*

†
Feijt, A., Jonker, H.   2000   Comparison of scaling parameters from spatial and temporal dis-
                                          tributions of cloud properties. *J. Geophys. Res.,* **105,** *29089–*
                                          29097

Graham, R. and Anderson, S.   1996   The relative utility of current observation systems to global-scale
                                          NWP forecasts; preliminary results, Workshop on the oper-
                                          ational use of scatterometer measurements of the ocean sur-
                                          face wind field, Alexandria Virginia, USA, April 22-23

Holton, James R.   1992   *An Introduction to Dynamic Meteorology.* third edition, Academic
                                          Press

Hoskins, B. J. and Valdes, P. J.   1990   On the existence of storm tracks. *J. Atmos. Sci.,* **47,** *1854–1864*

Kelly, G.   1997   Influence of observations on the operational ECMWF system
                                          ECMWF Newsletter (76)

Lorenc, A. C., Graham, R. J.,   1992   Preparation for the use of a Doppler wind lidar information in
   Dharssi, I., MacPherson, B.,   meteorological assimilation systems, *ESA-CR(P)-3454*
   Ingleby, N. B., Lunnon, R. W.

Marseille, G. J., Stoffelen, A.   1998   Study on the utility of a Doppler wind lidar for numerical weather
                                          prediction and climate. *ESA-CR 11982*

Marseille, G. J., Stoffelen, A.,   2002   LITE4ADM; On the Use of LITE data for the Atmospheric Dy-
   van Lammeren, A.   namics Mission - Aeolus. *KNMI internal report*

Morançais, D., Fabre, F.,   2002   ALADIN: the lidar instrument for the AEOLUS mission *SPIE*
   Schillinger, M., Culoma, A.   *Remote Sensing Conference, Symposium on Remote Sensing*
                                          Sensors, systems and next generation satellites VIII

Rapp, R. R., Schutz, C.,   1973   Cloud-free Line-of-Sight Calculations. *J. Appl. Meteorol.,* **12,**
   Rodriguez, E.   *484–493*

Reagan, J. A., McCormick, M. P.,   1989   Lidar sensing of aerosols and clouds in the troposphere and strato-
   Spinhirne, J. D.   sphere. *IEEE* **77,** *No3, 433–448*

Russel, P. B., Swissler, T. J.,   1979   Methodology for error analysis and simulation of lidar aerosol
   McCormick, M. P.   measurements. *Appl. Opt.* **18,** *No 22, 3783–3797*

Stephens, G. L.   1984   The parameterization of radiation for numerical weather predic-
                                          tion and climate models. *Mon. Weather Rev.,* **112,** *826–867*

Stoffelen, A., Flamant, P.,   2002   MERCI; Measurement Error Correlation Impact on the Atmos-
   Håkansson, M., Källén, E.,   pheric Dynamics Mission. *ESA-CR 15192/01/NL/MM*
   Marseille, G. J., Pailleux, J.,
   Schyberg, H., Vaughan, M.

Tiedtke, M.   1993   Representation of clouds in large-scale models. *Mon. Weather*
                                          Rev., **121,** *3040–3061*

Vaughan, J. M., Geddes, N. J.,   1998   Establishment of a backscatter coefficient and atmospheric
   Flamant, P. H., Flesia, C.   database. *ESA-CR, 12510/97/NL/RE*

Winker, D. M., Cough, R. H.,   1996   An overview of LITE: NASA's Lidar In-space Technology Exper-
   McCormick, M. P.   iment. *Proc. of the IEEE* **84,** *no.2*

Winker, D. M., Emmitt, G. D.   1997   Relevance of cloud statistics derived from LITE data to future
                                          Doppler wind lidars. *Proc. of the 9th conf. on Coherent Laser*
                                          Radar, Linköping

World Meteorological Organization   2001   Statement of Guidance Regarding How Well Satellite and *In*
                                          Situ Capabilities Meet WMO User Requirements in Several
                                          Application Areas. *WMO satellite reports SAT-26. WMO/TD*
                                          (1052)

† http://www.estec.esa.nl/explorer/documents/adm_sp1233_4.pdf